

# Isogeometric analysis based design of post-tensioned concrete beam towards construction-oriented topology optimization

Zixin Zhang<sup>1,2,3</sup>, Tejeswar Yarlaga<sup>1</sup>, Yao Zheng<sup>3</sup>, Liming Jiang<sup>1,2,\*</sup>, Asif Usmani<sup>1,2</sup>

<sup>1</sup> Department of Building Services Engineering, The Hong Kong Polytechnic University, Hung Hom, Hong Kong SAR

<sup>2</sup> Research Institute for Sustainable Urban Development, The Hong Kong Polytechnic University, Hung Hom, Hong Kong SAR

<sup>3</sup> School of Aeronautics and Astronautics, Zhejiang University, Zhejiang, China

**Abstract:** Topology optimization as a computational approach is used to find an optimal structure with specific objectives such as an ultimately lightweight design. The optimization is normally performed under a series of constraint functions to ensure expected structural performance for safety and resilience. To promote the use of topology optimization in structural engineering, it is crucially important to identify and apply suitable constraints for realistic construction. In this paper, a conceptual attempt aiming for a construction-oriented topology optimization framework is presented. An isogeometric analysis module using NURBS curves for geometric description and discretization is employed in stress analyses, which incorporates the density based SIMP optimization approach to generate the optimized topology. A Drucker-Prager criterion is adopted to constrain the stresses within the unequal limits of tension and compression for the use of concrete type material. To prevent slim components of potentially high complexity in construction, a minimum-width control is applied as an additional geometric control. In this paper, the conceptual framework is demonstrated using a prestressed concrete beam, while the optimization is performed to find suitable density distribution of concrete and a NURBS-described tendon profile after imposing the mapped prestressed action. The iterative optimization processes are presented and demonstrated to investigate the effect of tensile-compressive strength ratio and the minimum width, which reflects the construction-oriented vision pursuing a more regularized topology after applying the constraints in optimization.

**Keywords:** Isogeometric analysis, prestressed concrete structure, lightweight design, NURBS, minimum-width control.

## 1. Introduction

Topology optimization is a mathematical methodology for optimizing material distribution in a specific design domain, aiming to find an optimal topology corresponding to specific objectives and constraints. Since Bendsoe and Kikuchi (1988) presented a pioneering work of topology optimization, various numerical methods have been developed for this purpose, including density-based methods and evolutionary/genetic algorithms (Deaton and Grandhi

2014; Eschenauer and Olhoff 2001; Rozvany 2009; Sigmund and Maute 2013). As a typical density-based method, the Solid Isotropic Material with Penalization (SIMP) method is widely adopted in topology optimization. This approach was initially used in the automotive and aerospace industry, pursuing ultimately lightweight performance. In the recent decade, researchers intended to bring this computer-aided technique to the design of building and civil engineering structures (Beghini et al. 2015; Stromberg et al. 2011; Stromberg et al. 2012) to achieve the optimum distribution of structural materials in members. To bridge the gap between topology optimization and the realistic construction practice, it becomes crucially important to identify and apply practical constraints and performance goals, fulfilling the requirements for safety, resilience, and manufacturability of structural components.

For the optimized structure, structural material stresses should be ideally underneath the elastic limits, and the load-bearing capacity should be largely exploited. The Strut-and-Tie Modeling (STM) method was used in the topology optimization design for concrete structures to find an internal truss system representing the load transfer path (Almeida et al. 2013; Kwak and Noh 2006; Liang et al. 2000). Based on this concept, the density-based method was later used (Bruggi 2009; Bruggi 2010; Bruggi and Taliercio 2013) to generate the material layout to represent the STM model. Moreover, the Drucker-Prager stress constraint was later implemented by (Bruggi and Duysinx 2012) to represent the anisotropic behavior in tension and compression. The optimal design of reinforced concrete structure was later performed in a two-phase microstructure comprising steel rebar and concrete using Drucker-Prager stress constraints (Luo and Kang 2013). (Bogomolny and Amir 2012) considered the nonlinear elastoplastic behavior, and then developed approaches to consider the damage of concrete (Amir 2013; Amir and Sigmund 2013). The simultaneous optimization of the concrete continuum and reinforcement members were then presented (Amir 2013; Bruggi 2016; Gaynor et al. 2013), followed by a recently reported experimental evaluation of free-formed plain concrete (Jewett and Carstensen 2019). When considering different structural materials separately, a prestressed concrete beam with a steel tendon is a challenging topic. The actual prestressing effect is achieved using the configurational forces to optimize the single tendon layout (Eurviriyankul and Askes 2011). A simultaneous concrete topology and tendon shape optimization framework was presented by (Amir and Shakour 2018), which was validated using 3D printing concrete models (Vantighem et al. 2020).

Unlike the finite element-based method (FEM) widely adopted in analyzing the stress distribution (Jiang and Usmani 2018a; Jiang and Usmani 2018b), the Isogeometric Analysis (IGA) (Hughes et al. 2005) is an emerging approach. As pointed out in the milestone work of

Hughes et al.(2005), IGA was an extension of FEM and was inspired by the computer-aided design (CAD) methodology, featuring an exact geometric description from CAD by adopting Non-uniform Rational B-Splines (NURBS) as its basis functions. The IGA method enables identical description of the analysis model to the geometry model during optimization, as they both use the same NURBS parameters and the adaptive mesh for FEM could be avoided. The typical advantage of IGA-based structural topology optimization has been discussed by (Gao et al. 2019). Along with IGA, the aforementioned density-based SIMP method can be incorporated into the framework, as shown in Figure 1, in which a vision of construction-oriented topology optimization is proposed corresponding to the above-manifested needs. To implement topology optimization in a wider scope of realistic construction, the generated design of optimal topology should also be construction-friendly. Using NURBS based IGA model, the structural shape can be naturally compatible with the design input, which enables potential industrialized construction approaches such as factory prefabrication.

Moreover, the structural components of the optimal design should fulfil the safety and resilience requirements in a performance-based design domain. Ideally, the stresses of structural components should be maintained underneath specified limits in various loading scenarios (Jiang et al. 2021). It is also equally important that these components shall be of limited variation and easy-to-manufacture sections. Thus, geometry control, such as minimum width and tendon cover (discussed in this paper) and pattern control (future work), should be considered in the construction-oriented topology optimization framework.

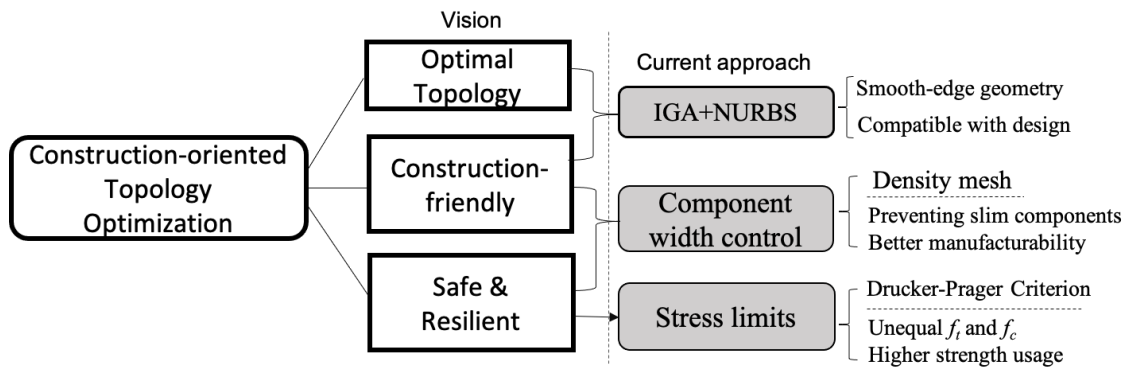


Figure 1 A vision of construction-oriented topology optimization

In this paper, a prestressed concrete beam with unequal tensile and compressive strengths and a tendon is used to demonstrate the vision of the construction-oriented topology optimization. The Drucker-Prager criterion is adopted in the optimization procedure to constrain the material stress within the realistic concrete strengths of low tensile strength and relatively high compressive strength. This is implemented with an IGA-SIMP topology

optimization framework, where a NURBS tendon curve representing equivalent prestress load is achieved using a simplified load mapping process from the tendon to the concrete (Section 3.3). A NURBS-based minimum-width control is applied to ensure manufacturability and prevent slim components for better resilience performance. The formulation and sensitivity analysis of the outlined optimization problem is discussed, followed by investigating various effects to the optimized topology, including the tensile-compressive strength ratio and the controlled component widths. Along with demonstration cases, the work presented in this paper seeks to develop a system of numerical approaches to port the topology optimization to the practical concerns of construction of civil engineering structures, which currently remains a starting step under the proposed vision and would be continuously developed with further studies.

## 2. NURBS based IGA method

### 2.1 The definition of NURBS

For a given knot vector, a monotonically increasing sequence  $\Xi = \{\xi_1, \xi_2, \dots, \xi_{n+p+1}\}$  in the parameter space defines the basis function, where  $n$  is the total number of basis functions and  $p$  is the polynomial order. In Cox-de Boor recursive format (Piegl and Tiller 2012), the B-spline basis function is defined as:

$$N_{i,0}(\xi) = \begin{cases} 1, & \text{if } \xi_i \leq \xi \leq \xi_{i+1} \\ 0, & \text{otherwise} \end{cases}$$

$$N_{i,p}(\xi) = \frac{\xi - \xi_i}{\xi_{i+p} - \xi_i} N_{i,p-1}(\xi) + \frac{\xi_{i+p+1} - \xi}{\xi_{i+p+1} - \xi_{i+1}} N_{i+1,p-1}(\xi), \quad (1)$$

$$(i = 1, 2, \dots, n + p + 1)$$

Therefore, a NURBS curve can be defined as:

$$C(\xi) = \frac{\sum_{i=1}^n N_i^p(\xi) \omega_i \mathbf{P}_i}{\sum_{j=1}^n N_j^p(\xi) \omega_j} = \sum_{j=1}^m R_i^p(\xi) \mathbf{P}_i \quad (2)$$

where  $\mathbf{P}_i$  represents the coordinates of the  $i$ -th control points.  $\omega_i$  indicates the weight of  $\mathbf{P}_i$  associated with the  $p$ -th order B-spline basis function  $N_i^p(\xi)$ , which is shown in Figure 2. For simplicity, the NURBS basis function is denoted as  $R_i^p(\xi)$  in this paper.

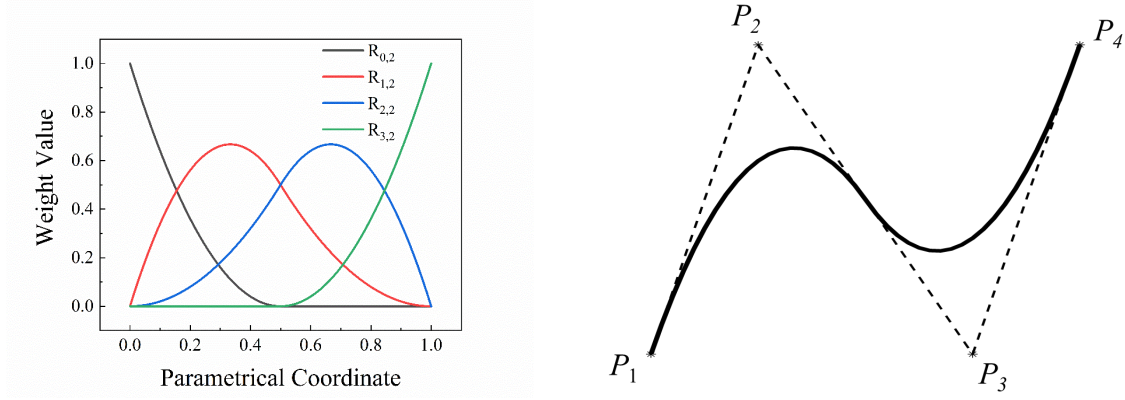


Figure 2 Example of (a) the basis function; (b) a NURBS curve with  $\omega=[1,1,1,1]$

## 2.2 IGA-SIMP method

The IGA employs NURBS to describe the geometry and to discretize the model for structural analyses. The shape function using NURBS is expressed as:

$$\mathbf{x}(\xi, \eta) = \sum_{i=1}^n \sum_{j=1}^m R_{i,j}^{p,q}(\xi, \eta) \mathbf{x}_{i,j} \quad (3)$$

where  $R_{i,j}^{p,q}(\xi, \eta)$  is the NURBS surface basis function and  $\mathbf{x}_{i,j}$  denotes the vector of variables, such as the coordinates, displacement, or density value of the control point. The governing equation of isogeometric structural analyses remains the classic form:

$$\mathbf{K}\mathbf{u} = \mathbf{F} \quad (4)$$

where  $\mathbf{K}$  is the global stiffness matrix.  $\mathbf{u}$  is the global displacement vector and  $\mathbf{F}$  is the load vector.  $\mathbf{K}$  is formulated from the elemental stiffness matrices of IGA:

$$\mathbf{K} = \sum_e \mathbf{K}_e \quad (5)$$

The element stiffness matrix of planar structure  $\mathbf{K}_e$  can be expressed as:

$$\begin{aligned} \mathbf{K}_e &= \int_{\Omega_e} \mathbf{B}_e^T \mathbf{D}_e \mathbf{B}_e d\Omega_e \\ \mathbf{D}_e &= (\rho_e^p + \rho_{\min}) \mathbf{D}_0 \end{aligned} \quad (6)$$

where  $\mathbf{B}_e$  is the strain-displacement matrix,  $\mathbf{D}_e$  the elemental elastic matrix,  $\mathbf{D}_0$  the solid elastic matrix.  $p$  is the penalty coefficient to penalize the intermediate density, generally set as 3 (Rozvany 2009), while  $\rho_{\min}$  is the minimum density value (generally as 0.001) to avoid numerical instability as  $\rho_e$  is close to zero. The density in the element centroid is approximately set to be the elemental density  $\rho_e$ , which can be calculated as:

$$\rho_e = \sum_{i=1}^n \sum_{j=1}^m R_{i,j}^{p,q}(\xi_e^c, \eta_e^c) \rho_{i,j} \quad (7)$$

$\xi_e^c, \eta_e^c$  are the parametric coordinates of the  $e$ -th element center. For the plane stress problem, the stress vector of point  $a$  is expressed as below:

$$\boldsymbol{\sigma}_a = \rho_e^s \mathbf{D}_0 \mathbf{B}_a \mathbf{u}_e \quad (8)$$

where  $\mathbf{B}_a$  is the strain-displacement matrix of point  $a$  and  $\mathbf{u}_e$  is the displacement of the element control point.  $s$  is generally set as 0.5 (Yang et al. 2018) to penalize the intermediate density value.

### 3. Modelling post-tensioned concrete beams using IGA

A post-tensioned concrete beam is optimized using the proposed construction-oriented topology optimization framework as a typical structure comprising separate components of different materials. Based on the equivalent load method (Moorman 1952), a set of equivalent loads can replace the prestress effect. A new load transfer formulation of the continuous equivalent prestress load is developed for the IGA-SIMP framework, enabling the prestressed concrete beam's optimization procedure.

#### 3.1 IGA for prestressed beam

For the concrete part of a simply supported prestressed concrete beam, it is subjected to various types of loads, which includes the external loads such as vehicles and structural self-weight as well as the equivalent loads representing the action of the prestressed tendon. The displacement caused by the equivalent prestress  $\mathbf{u}_{pre}$  will balance the displacement caused by external load and self-weight load  $\mathbf{u}_{ext}$ ,  $\mathbf{u}_{sw}$ . Similar to the finite element method, the equilibrium of the prestressed beam can be formulated as below:

$$\mathbf{K} \mathbf{u}_{total} = \mathbf{F}^{ext} + \mathbf{F}^{sw} + \mathbf{F}^{pre} + \mathbf{F}^{pre*} \quad (9)$$

where  $\mathbf{F}^{ext}$  and  $\mathbf{F}^{sw}$  represent the external force vector and the self-weight force vector, respectively. The tendon geometry is described using a NURBS curve with equidistant  $x$  coordinates and the varying  $y$  coordinates of control points. A smooth curve across the concrete beam can be thereafter assigned to the tendon, as shown in Figure 3(a). The prestressed load due to the tendon comprises two parts: equivalent distributed load along the tendon  $\mathbf{F}^{pre}$  and concentrated anchor load  $\mathbf{F}^{pre*}$ , as shown in Figure 3(b). It should be noted that the prestress loss during construction and tendon friction is ignored in this model.

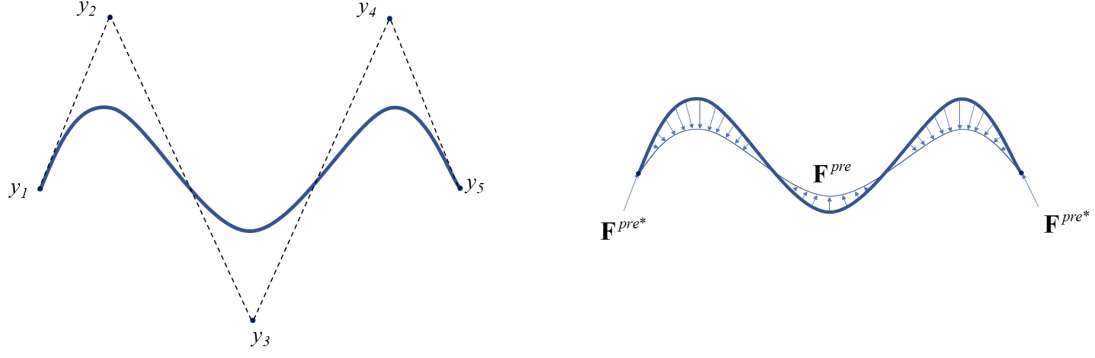


Figure 3 Tendon of the prestressed beam: (a) Tendon curve using NURBS (b) load due to prestressed tendon

### 3.2 Equivalent prestressed load along the tendon

The equivalent distributive prestressed load is calculated according to the curvature of the tendon, irrespective of the shape of the member and support condition. The distributed load along the tendon is expressed as:

$$\mathbf{q}(\xi) = q(\xi) \mathbf{n}(\xi) \quad (10)$$

where  $q(\xi) = \kappa(\xi) \cdot T_{pre}$  describes the curvature-based load distribution along the tendon, and  $\mathbf{n}(\xi)$  is the corresponding normal direction.  $T_{pre}$  indicates the prestressed force and  $\kappa(\xi)$  is the curvature. According to the principle of virtual work, the distributed load could be equivalented as a load vector on control points:

$$\mathbf{F}^{ten} \mathbf{u}^{ten} = \int \mathbf{q}(\xi) \cdot \mathbf{u}(\xi) ds \quad (11)$$

where  $\mathbf{F}^{ten}$  and  $\mathbf{u}^{ten}$  are the load vector and the displacement vector at the tendon control point, respectively. The equivalent load using Gaussian integration is expressed as follows:

$$\mathbf{F}^{ten} = \sum_e \sum_{i=1}^{N_{GP}^{ten}} w_i \mathbf{q}_i R_i^{ten} |\mathbf{J}_1^{ten}| |\mathbf{J}_2^{ten}| \quad (12)$$

where  $N_{GP}^{ten}$  is the number of tendon elemental gaussian points.  $\mathbf{J}_1^{ten}$  is the tendon elemental Jacobian matrix from the parametric space to the physical space, while  $\mathbf{J}_2^{ten}$  is the parent space of the gaussian point to the parametric space.  $w_i$  represents the weight value of  $i$ -th gaussian point in  $e$ -th tendon element.

It should be noted that the initial number of control points of tendon shape is limited, which would lead to an inaccurate estimation of the equivalent prestressed in the mapping process, as shown in Figure 4. By introducing the h-refinement (Piegl and Tiller 2012), more knots and control points can be automatically added into the curve to improve the accuracy with consistent geometry at the model formulation stage. In order to insert the new knot

$\bar{\xi} \in [\xi_k, \xi_{k+1}]$  into the knot vector, the new  $n+1$  control point vector  $\{\bar{\mathbf{P}}_1, \bar{\mathbf{P}}_2, \dots, \bar{\mathbf{P}}_{n+1}\}$  is expressed using the following equation:

$$\bar{\mathbf{P}}_i = \alpha_i \mathbf{P}_i + (1 - \alpha_i) \mathbf{P}_{i-1}$$

$$\alpha_i = \begin{cases} 1, & i \leq k - p, \\ \frac{\bar{\xi} - \xi_i}{\xi_{i+p} - \xi_i}, & k - p + 1 \leq i \leq k, \\ 0, & i \geq k + 1. \end{cases} \quad (13)$$

The refined set of control points set can be thereafter attained, as shown in Figure 5. To simplify the expression of h-refinement sensitivity analysis in Section 5.1, the relationship between the coordinates of refined and original control points in Eq. (13) could be explicitly rewritten as follows:

$$\mathbf{P}_i^{refine} = \sum_{j=1}^{N_{initial}} W_{i,j}^{refine} \mathbf{P}_j^{initial} \quad (14)$$

where  $W_{i,j}^{refine}$  indicates the weight value from  $j$ -th original control point to  $i$ -th refined control point. These added control points can thereafter refine the sensitivity description of tendon shape variables during optimization, as shown in Eq. (31).

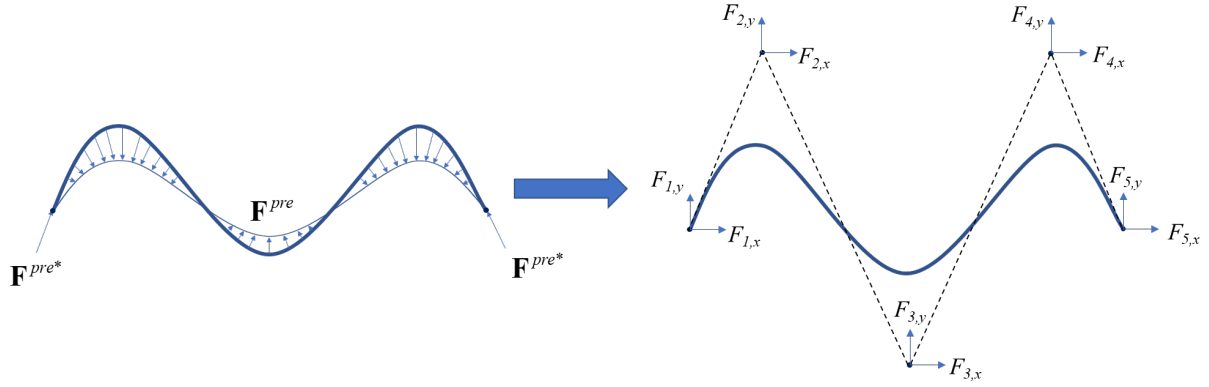


Figure 4 tendon prestressed load mapping process

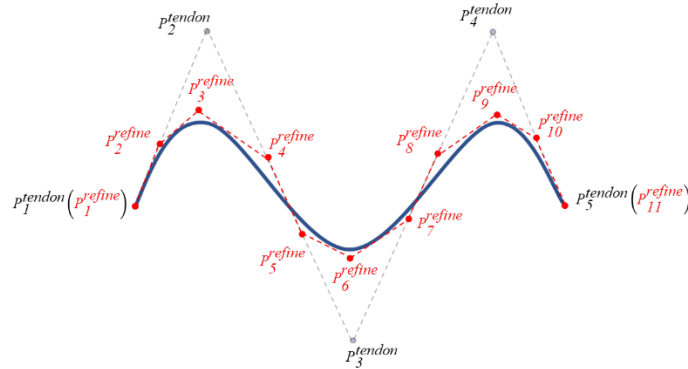


Figure 5 the h-refinement of tendon control point



For the axial load at both ends of the prestressed tendon, it is also applied along the tangential direction at the end of the tendon curve, as shown below:

$$\mathbf{F}^{ten*} = T_{pre} \cdot \mathbf{n}^* \quad (15)$$

where  $\mathbf{n}^*$  indicates the tangential direction of the tendon curve end;  $T_{pre}$  is the prestressed load value.

### 3.3 Load mapping scheme from tendon to concrete

The load mapping scheme of the prestressed concrete beam optimization can take advantage of using IGA. To address the prestress load on the concrete section, a mapping scheme is applied to transform physical coordinates to parametrical coordinates of the concrete domain. Traditionally in FEA, the process is achieved by calculating inverse Jacobian matrix for each finite element. While in IGA framework, an direct and explicit relationship (Costa et al. 2019) between physical coordinates and parametrical coordinates can be applied. The differences of these two approaches are illustrated in Figure 6. The transformation from the physical coordinate of tendon control points to the concrete domain can be expressed as follows:

$$\xi_i^{con} = \frac{P_i^x}{L}, \eta_i^{con} = \frac{P_i^y}{D} \quad (16)$$

where  $P_i^x, P_i^y$  are physical coordinates of the  $i$ -th tendon control point, and  $\xi_i^{con}, \eta_i^{con}$  are the corresponding parametrical location in the concrete domain. The load mapping operation based on this geometric transformation is illustrated in Figure 7. According to the principle of virtual work, the equivalent prestressed load can be written as follows:

$$\begin{aligned} \mathbf{F}_j^{pre} &= \sum_{i=1}^{N_{con}} \mathbf{F}_i^{ten} R_{(\xi_i^{con}, \eta_i^{con})}^{con}(\xi_j, \eta_j) = \sum_{i=1}^{N_{con}} \mathbf{F}_i^{ten} R_i^{con}(j) \\ \mathbf{F}_j^{pre*} &= \sum_{i=1}^n \mathbf{F}_i^{ten*} R_i^{con}(j) \end{aligned} \quad (17)$$

where  $R_{(\xi_i^{con}, \eta_i^{con})}^{con}(\xi_j, \eta_j)$  (alternatively denoted as  $R_i^{con}(j)$  for simplicity) represents the NURBS basis function, which maps the parametric location of the tendon control point  $(\xi_i^{con}, \eta_i^{con})$  to the concrete control point  $(\xi_j, \eta_j)$ .

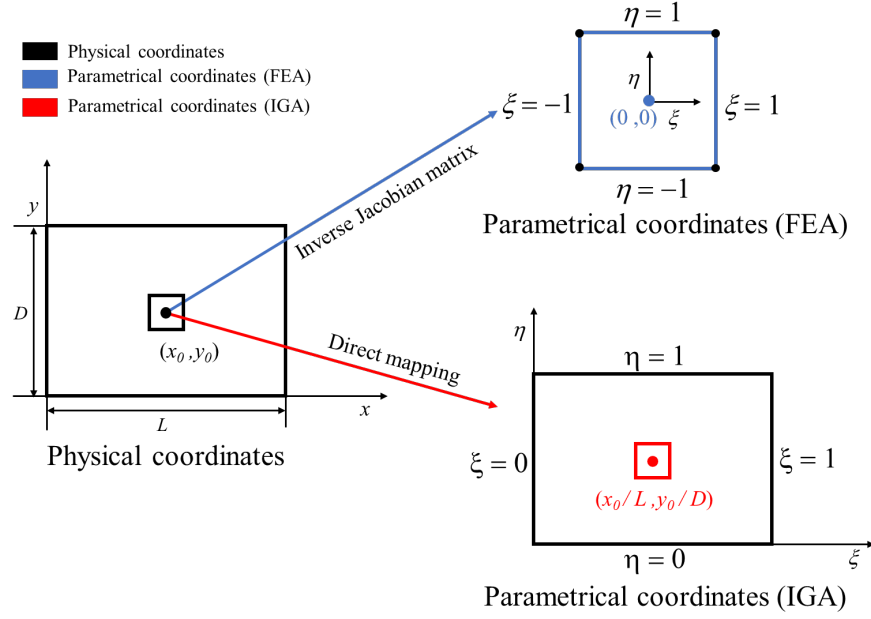


Figure 6 The relationship of physical coordinates and parametrical coordinates in FEA and IGA.

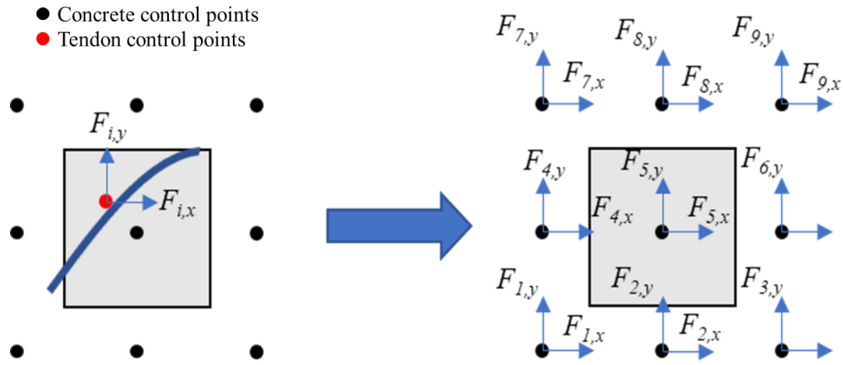


Figure 7 The inverse mapping process of an equivalent load from the tendon to the concrete domain

## 4. Optimization Problem formulation

### 4.1 Formulation of IGA-SIMP optimization with stress constraints

As previously explained, stress constraints are implemented in the IGA-SIMP optimization framework. For structural materials like concrete, the Drucker-Prager stress criterion is more suitable to exploit the unequal material strengths in tension and compression than the Von-Mises criterion of identical stress limits (Liu et al. 2018). The Drucker-Prager criterion is usually written as below:

$$F(\boldsymbol{\sigma}) = \alpha I_1(\boldsymbol{\sigma}) + \sqrt{J_2(\boldsymbol{\sigma})} - H \quad (18)$$

where  $I_1, J_2$  indicate the first and second invariant of the stress tensor, respectively.  $a$  and  $H$  are variables and can be calculated with compressive strength  $\sigma_c$  and tensile strength  $\sigma_t$ :

$$\begin{aligned}\alpha &= \frac{\sigma_c - \sigma_t}{\sqrt{3}(\sigma_c + \sigma_t)} \\ H &= \frac{2\sigma_c\sigma_t}{\sqrt{3}(\sigma_c + \sigma_t)}\end{aligned}\tag{19}$$

Along with the Drucker-Prager criterion, the IGA-SIMP topology optimization can be formulated as:

$$\begin{aligned}\min_{[\rho, y]} \quad & V = \sum_{e=1}^{N_e} (\rho_e + \rho_{\min}) V_e \\ \text{s.t.} \quad & \mathbf{K}\mathbf{u}_{total} = \mathbf{F}^{ext} + \mathbf{F}^{sw} + \mathbf{F}^{pre} + \mathbf{F}^{pre*} \\ & \alpha I_1(\boldsymbol{\sigma}) + \sqrt{J_2(\boldsymbol{\sigma})} - H \leq 0 \\ & 0 \leq \rho_e \leq 1, \quad e = 1, \dots, N_e \\ & t \leq y_i \leq h - t, \quad i = 1, \dots, N_{initial}\end{aligned}\tag{20}$$

The optimization is herein performed regarding the concrete topology and tendon shape.  $[\rho, y]$  as the design variables of the optimization model represents the density of concrete ( $\rho$ ) at control points and the  $y$  coordinate of the tendon curve.  $N_e, N_{initial}$  are the number of concrete element and initial tendon control points, respectively.  $h$  is the total beam height, and  $t$  is the interval of the unreachable region of the tendon, as illustrated in Figure 8.

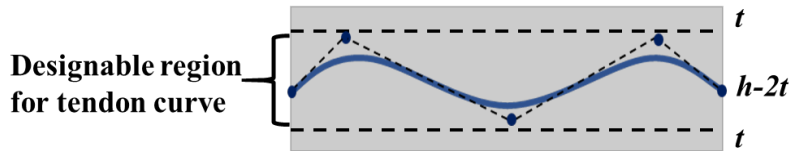


Figure 8 Designable region for tendon curve

## 4.2 Refinement of stress constraint

For stress constraint problem, the following numerical issues have to be carefully resolved: (1) the stress singularity problem; (2) the unaffordable computational cost of numerous local stress constraints; and (3) the optimization stabilization. Various approaches are used to alleviate the above technical barriers, which have been briefly explained in this section.

For issue (1): when the density of the element tends to be zero, it will result in extremely large stress and violate the yield criterion. Consequently, the yield constraints in the low-density region will prevent materials from being completely removed, leading to numerical

difficulty obtaining the actual optimal material distribution. This phenomenon is usually termed as stress singularity, which is alleviated using an epsilon-relaxation method (Cheng and Guo 1997) in this paper:

$$\begin{aligned}\varphi_{F,e}(\boldsymbol{\sigma}_e, \rho_e) &= \frac{1}{h_e} \left( \alpha I_1(\boldsymbol{\sigma}_e) + \sqrt{J_2(\boldsymbol{\sigma}_e)} \right) / H \leq 1 \\ h_e &= 1 + \frac{\varepsilon}{\rho_e} - \varepsilon, \quad (e = 1, 2, \dots, N_e)\end{aligned}\tag{21}$$

where  $h_e$  is the relaxation coefficient representing the relaxation degree of the corresponding constraint and  $\varepsilon$  is a prescribed small positive real number. A greater value means a higher relaxation degree.

For issue (2): The computational cost of implementing stress constraints for the elements of the model is a technical challenge during the optimization process. This issue is addressed by wrapping the local constraints as a single global constraint using the Kreisselmeier-Steinhauser (K-S) and p-norm stress measure (Duysinx and Sigmund 1998; Verbart et al. 2017; Yang and Chen 1996) to reduce the computational complexity. The major difference between these two global constraint functions is that P-norm requires non-negative local function value, while K-S has no such requirements (Yang et al. 2018). Due to the negative values of the Drucker-Prager criterion, the K-S function is chosen as the aggregation function:

$$G_{KS}(\boldsymbol{\rho}, \mathbf{y}) = \frac{1}{\eta} \ln \sum_e^N \exp(\eta \varphi_{F,e}(\boldsymbol{\sigma}_e, \rho_e)) \leq 1\tag{22}$$

where  $\varphi_{F,e}(\boldsymbol{\sigma}_e, \rho_e)$  is the relaxation function in Eq. (21), and  $\eta > 0$  is the aggregation parameter, which is used to penalize the violation of the local constraints. By increasing the value of the aggregation parameter  $\eta$ , the approximation error could be reduced. However, the larger  $\eta$  also leads to higher nonlinearity, which means more difficulty of convergence.

For issue (3), the STM-based stress correction scheme (Yang et al. 2018) is used to correct the global stress measures and to stabilize the optimization process with the oscillation control, as shown in Eq.(23).

$$\tilde{G}_{KS} = cp \bullet G_{KS}\tag{23}$$

$cp$  is the correction parameter, as:

$$cp_n = \begin{cases} \frac{\max(\varphi_{F,e})_n}{(G_{KS})_n}, & n = 1 \\ q_n \frac{\max(\varphi_{F,e})_n}{(G_{KS})_n} + (1 - q_n)cp_{n-1}, & n > 1 \end{cases} \quad (24)$$

where the control factor ( $0 < q_n < 1$ ) is to alleviate the discontinue change of  $cp_n$  and to avoid iterative oscillation leading to unstable convergence.

### 4.3 Geometry control of the optimum model

Aiming for construction-oriented topology optimization, the design variables, including the minimum width (length scale) control and the tendon-concrete filter, are necessary to be included in order to prevent segments of low manufacturability, as illustrated in Figure 9. For instance, very slim components are challenging to manufacture and of little resilience during life-time service. This optimal design effect is avoided by a desirable width control method to set up a minimum width. A NURBS-based minimum length scale control approach (Costa et al. 2019) is adopted in this paper and further developed to co-work with the IGA-SIMP optimization framework. Besides the geometric mesh, an independent density mesh is used to control the minimum length (width) scale. The density filter can be thereafter similarly formulated as Eq. (7) and can be written as below:

$$\rho_e = \sum_{j \in N_i} R_j^{den}(e) \rho_j \quad (25)$$

where  $R_j^{den}(i)$  is the NURBS rational basis function of density variables.

Moreover, a tendon-concrete filter is used to ensure the minimum cover of the tendon by the concrete. The filter proposed by (Amir and Shakour 2018) can be expressed as follows:

$$\hat{\rho}_e = \rho_e + (1 - \rho_e) e^{-\frac{1}{2} \left( \frac{d_{ei}}{\beta_{fil}} \right)^{\mu_{pre}}} \quad (26)$$

where  $\hat{\rho}_e$  means the  $e$ -th elemental density and  $d_{ei}$  indicates the shortest distance between the center of  $e$ -th element and the tendon control points.  $\beta_{fil}$  is the function width, while  $\mu_{pre}$  is the sharpness of the Super-Gaussian function.

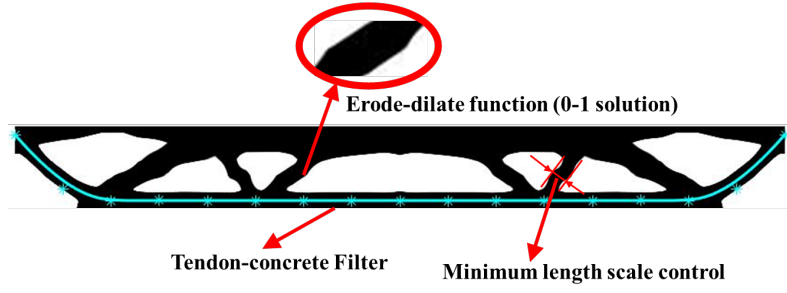


Figure 9 illustration of geometry control

Finally, the erode-dilate function (Lazarov et al. 2016) is applied to obtain the clear 0-1 solution. the formulation of erode-dilate method is as follows:

$$\begin{aligned}\tilde{\rho}_e^{ero} &= \frac{\tanh(\beta_{HS}\eta_{ero}) + \tanh(\beta_{HS}(\hat{\rho}_e - \eta_{ero}))}{\tanh(\beta_{HS}\eta_{ero}) + \tanh(\beta_{HS}(1 - \eta_{ero}))} \\ \tilde{\rho}_e^{dil} &= \frac{\tanh(\beta_{HS}\eta_{dil}) + \tanh(\beta_{HS}(\hat{\rho}_e - \eta_{dil}))}{\tanh(\beta_{HS}\eta_{dil}) + \tanh(\beta_{HS}(1 - \eta_{dil}))}\end{aligned}\quad (27)$$

As the sharpness value  $\beta_{HS}$  increases, the 0-1 solution is better, but it reduces the stability of the optimization iteration.  $\eta_{ero}$  and  $\eta_{dil}$  are the projection threshold for eroded and dilated design (Lazarov et al. 2016), respectively. It should be noted that too high or too low projection thresholds can produce Zig-Zag boundaries since the NURBS-based length scale method reduces the topological design space. As shown in Figure 10, a zoomed  $3 \times 3$  nodes region using different projection schemes is presented. The boundary of density distribution is not sharp enough if no Heaviside is adopted (Figure 10(a)), whereas the Heaviside method of a zero projection leads to a Zig-Zag boundary. When the projection threshold is defined as a variable similar to the erode-dilate method (Lazarov et al. 2016), a relatively smooth boundary can be obtained.

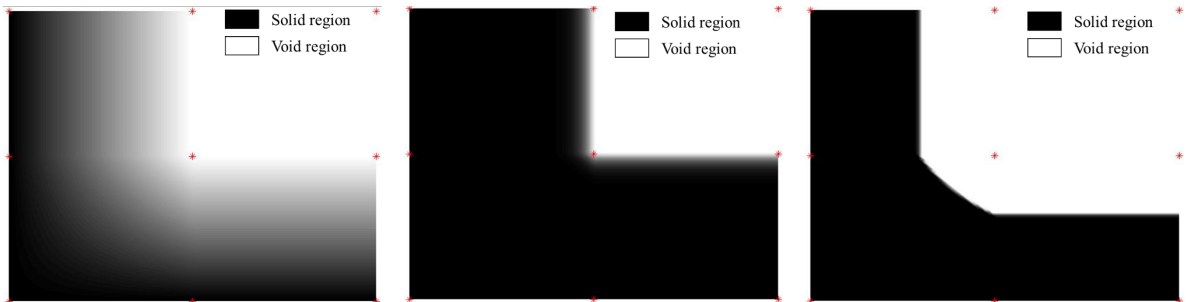


Figure 10 Comparison of projection schemes with different project threshold,  $(\eta_{ero}, \eta_{dil})$ : (a) no Heaviside; (b) projection threshold is 0; (c) variable projection threshold e.g.: (0.4, 0.6).

## 5. Sensitivity analysis

### 5.1 Volume sensitivity

The material distribution of concrete is described with the topological variables of concrete and shape variables of the tendon. The volume objective and the stress constraint are coupled during the topology optimization, which eventually produces the design variables  $\mathbf{x}=[\boldsymbol{\rho},\mathbf{y}]$ . For the derivation of volume objective function Eq. (20), the partial derivative for the design variable  $x_i$  can be given using a direct form:

$$\frac{\partial V}{\partial x_i} = \sum_e \frac{\partial \tilde{\rho}_e}{\partial x_i} V_e \quad (28)$$

The explicit gradient of the term  $\frac{\partial \tilde{\rho}_e}{\partial x_i}$  is calculated from the partial derivatives of the topological variables  $\rho_i$ :

$$\frac{\partial \tilde{\rho}_e}{\partial \rho_i} = \frac{\partial \tilde{\rho}_e}{\partial \hat{\rho}_e} \frac{\partial \hat{\rho}_e}{\partial \rho_e} \frac{\partial \rho_e}{\partial \rho_i} \quad (29)$$

In Eq. (29), the derivatives of variables can be explicitly computed as follows: (i)  $\frac{\partial \tilde{\rho}_e}{\partial \hat{\rho}_e}$  is derived from the Heaviside function in Eq. (27); (ii)  $\frac{\partial \hat{\rho}_e}{\partial \rho_e}$  is a differential form of the tendon-concrete filter in Eq. (26); (iii)  $\frac{\partial \rho_e}{\partial \rho_i}$  is derived from Eq. (25), where the derivatives of the NURBS filter from density design variables to elemental density. Particularly the partial derivative of  $\tilde{\rho}_e$  with respect to the shape variable  $y_i$  is given as below:

$$\frac{\partial \tilde{\rho}_e}{\partial y_i} = \frac{\partial \tilde{\rho}_e}{\partial \hat{\rho}_e} \frac{\partial \hat{\rho}_e}{\partial d_{ei}} \frac{\partial d_{ei}}{\partial y_i} \quad (30)$$

where  $\frac{\partial \hat{\rho}_e}{\partial d_{ei}}$  is derived from the Heaviside function in Eq. (27) and  $\frac{\partial d_{ei}}{\partial y_i}$  is based on the Euclidean distance. According to the h-refinement operation in Eq. (14), the distance is computed from the element center to the refined tendon control points and then being projected to shape variables  $y_i$ , as shown in the following form:

$$\frac{\partial d_{ei}}{\partial y_i} = \frac{\partial d_{ei}}{\partial y_j^{refine}} \frac{\partial y_j^{refine}}{\partial y_i} \quad (31)$$

Where the first component  $\frac{\partial d_{ei}}{\partial y_j^{refine}}$  is derived from the formula of distance, it should be noted

that the derivatives of the non-closest control points are zero. Regarding the second component,  $\frac{\partial y_j^{refine}}{\partial y_i}$  is given by Eq. (14).

## 5.2 Stress constraint sensitivity

For the stress constraint function, the adjoint method is used for sensitivity analysis, which is expressed as follows:

$$\phi(\mathbf{p}, \mathbf{y}) = \tilde{G}_{KS} + \boldsymbol{\lambda}^T (\mathbf{K} \mathbf{u}_{total} - \mathbf{F}_{ext} - \mathbf{F}_{sw} - \mathbf{F}_{pre} - \mathbf{F}_{pre}^*) \quad (32)$$

where  $\boldsymbol{\lambda}$  is the adjoint vector. The partial derivative of Eq. (32) to a certain variable  $x_i$  is given by:

$$\begin{aligned} \frac{\partial \phi}{\partial x_i} = & \frac{\partial \tilde{G}_{KS}}{\partial \varphi_{F,e}} \left( \frac{\partial \varphi_{F,e}}{\partial \boldsymbol{\sigma}} \frac{\partial \boldsymbol{\sigma}}{\partial \rho_e} \frac{\partial \rho_e}{\partial x_i} + \frac{\partial \varphi_{F,e}}{\partial \boldsymbol{\sigma}} \frac{\partial \boldsymbol{\sigma}}{\partial \mathbf{u}_{total}} \frac{\partial \mathbf{u}_{total}}{\partial x_i} + \frac{\partial \varphi_{F,e}}{\partial h_e} \frac{\partial h_e}{\partial \rho_e} \frac{\partial \rho_e}{\partial x_i} \right) \\ & + \boldsymbol{\lambda}^T \left( \frac{\partial \mathbf{K}}{\partial x_i} \mathbf{u}_{total} + \mathbf{K} \frac{\partial \mathbf{u}_{total}}{\partial x_i} - \frac{\partial \mathbf{F}_{sw}}{\partial x_i} - \frac{\partial \mathbf{F}_{pre}}{\partial x_i} - \frac{\partial \mathbf{F}_{pre}^*}{\partial x_i} \right) \end{aligned} \quad (33)$$

To eliminate the implicit term  $\frac{\partial \mathbf{u}_{total}}{\partial x_i}$ , by collecting all the related terms in Eq. (33), the following adjoint equation is to be solved:

$$\frac{\partial \tilde{G}_{KS}}{\partial \varphi_{F,e}} \frac{\partial \varphi_{F,e}}{\partial \boldsymbol{\sigma}} \frac{\partial \boldsymbol{\sigma}}{\partial \mathbf{u}_{total}} + \boldsymbol{\lambda}^T \mathbf{K} = 0 \quad (34)$$

Where  $\frac{\partial \tilde{G}_{KS}}{\partial \varphi_{F,e}}$  is calculated by the K-S aggregation function in Eq. (23), and  $\frac{\partial \varphi_{F,e}}{\partial \boldsymbol{\sigma}}$  can be

obtained from Eq. (21), which is related to the stress relaxation procedure. The last term  $\frac{\partial \boldsymbol{\sigma}_e}{\partial \mathbf{u}_e}$

is derived from Eq. (8), for measuring the elemental stresses. Then, by solving the Eq. (34), the adjoint vector  $\boldsymbol{\lambda}$  is obtained. After plugging it into Eq. (33), the expression of Eq. (33) can be rewritten as:

$$\begin{aligned} \frac{\partial \phi}{\partial x_i} = & \frac{\partial \tilde{G}_{KS}}{\partial \varphi_{F,e}} \left( \frac{\partial \varphi_{F,e}}{\partial \boldsymbol{\sigma}} \frac{\partial \boldsymbol{\sigma}_e}{\partial \rho_e} \frac{\partial \rho_e}{\partial x_i} + \frac{\partial \varphi_{F,e}}{\partial h_e} \frac{\partial h_e}{\partial \rho_e} \frac{\partial \rho_e}{\partial x_i} \right) \\ & + \boldsymbol{\lambda}^T \left( \frac{\partial \mathbf{K}}{\partial x_i} \mathbf{u}_{total} - \frac{\partial \mathbf{F}_{sw}}{\partial x_i} - \frac{\partial \mathbf{F}_{pre}}{\partial x_i} - \frac{\partial \mathbf{F}_{pre}^*}{\partial x_i} \right) \end{aligned} \quad (35)$$



The unknown derivatives in Eq. 35 can be explicitly obtained as follows: (i)  $\frac{\partial \boldsymbol{\sigma}_e}{\partial \rho_e}$  is obtained

from the stress expression in Eq. (8); (ii)  $\frac{\partial \varphi_{F,e}}{\partial h_e}$  and  $\frac{\partial h_e}{\partial \rho_e}$  are calculated from the stress

relaxation function in Eq. (21); (iii)  $\frac{\partial \mathbf{K}}{\partial x_i}$  is based on the interpolation rule of the stiffness

matrix in Eq. (5); (iv) For  $\frac{\partial \mathbf{F}_{sw}}{\partial x_i}$ , the self-weight load is expressed as

$\mathbf{F}_{sw} = \sum_e \sum_{i \in e} w_i R_i^{con} \rho_e \mathbf{g} |\mathbf{J}_1| |\mathbf{J}_2|$ , which suggests the derivative can be given as:

$$\frac{\partial \mathbf{F}_{sw}}{\partial x_i} = \sum_e \sum_{i \in e} w_i R_i^{con} \frac{\partial \rho_e}{\partial x_i} \mathbf{g} |\mathbf{J}_1| |\mathbf{J}_2| \quad (36)$$

(v) The derivatives of the prestress force vectors  $\frac{\partial \mathbf{F}_{pre}}{\partial x_i}$ ,  $\frac{\partial \mathbf{F}_{pre}^*}{\partial x_i}$  are only related to shape variables (i.e., geometry of the tendon). The derivatives of distributive prestress load can be given as below:

$$\frac{\partial \mathbf{F}_{pre}}{\partial y_i} = \left[ \sum_e \sum_{j=1}^{N_{GP}^{ten}} \left( w_j \frac{\partial \mathbf{q}_j}{\partial y_i} R_j^{ten} |\mathbf{J}_1^{ten}| |\mathbf{J}_2^{ten}| + w_j \mathbf{q}_j R_j^{ten} \frac{\partial |\mathbf{J}_1^{ten}|}{\partial y_i} |\mathbf{J}_2^{ten}| \right) \right] \mathbf{R}^{con} + \left( \sum_e \sum_{j=1}^{N_{GP}^{ten}} w_j \mathbf{q}_j R_j^{ten} |\mathbf{J}_1^{ten}| |\mathbf{J}_2^{ten}| \right) \frac{\partial \mathbf{R}^{con}}{\partial y_i} \quad (37)$$

(i) From Eq. (10),  $\frac{\partial \mathbf{q}_j}{\partial y_i} = \frac{\partial q_j}{\partial y_i} \mathbf{n}_j + q_j \frac{\partial \mathbf{n}_j}{\partial y_i}$  and  $\frac{\partial q_j}{\partial y_i} = \frac{\partial \kappa_j}{\partial y_i} T_{pre}$  can be calculated. For the

derivatives of curvature  $\frac{\partial \kappa_j}{\partial y_i}$  and normal direction  $\frac{\partial \mathbf{n}_j}{\partial y_i}$ , please refer to the detailed

explanation in Appendix 8.1 and 8.2;

(ii)  $\frac{\partial |\mathbf{J}_1^{ten}|}{\partial y_i}$  is also available in the process of derivation of the normal direction in Appendix

8.2, as described in Eq. (49);

(iii) For the last term  $\frac{\partial \mathbf{R}_j^{con}(k)}{\partial y_i} = \frac{\partial \mathbf{R}_j^{con}(k)}{\partial \eta_j^{con}} \frac{\partial \eta_j^{con}}{\partial y_j^{refine}} \frac{\partial y_j^{refine}}{\partial y_i}$ ,  $\frac{\partial \mathbf{R}_j^{con}(k)}{\partial \eta_j^{con}}$  is the first-order

derivatives of NURBS surface in Eq. (17), while  $\frac{\partial \eta_j^{con}}{\partial y_j^{refine}}$  is from the physical and

parametrical coordinates relation in Eq. (16) and  $\frac{\partial y_j^{refine}}{\partial y_i}$  is available in Eq. (31).

The partial derivate of the concentrated prestressed load  $\frac{\partial \mathbf{F}_{pre}^*}{\partial y_i}$  is given as:

$$\frac{\partial \mathbf{F}_{pre}^*}{\partial y_i} = \frac{\partial \mathbf{F}_{ten}^*}{\partial y_i} \mathbf{R}^{con} + \mathbf{F}_{ten}^* \frac{\partial \mathbf{R}^{con}}{\partial y_i} \quad (38)$$

where  $\frac{\partial \mathbf{R}^{con}}{\partial y_i}$  is already available and  $\frac{\partial \mathbf{F}_{ten}^*(\xi)}{\partial y_i}$  can be obtained from Eq. (15). The

corresponding tangential derivation term  $\frac{\partial \mathbf{n}^*(\xi)}{\partial y_i}$  is given in Eq. (45) in Appendix 8.2.

## 6. Numerical demonstration

The proposed topology optimization framework is demonstrated using a simply-supported post-tensioned concrete beam, as shown in Figure 11, where a half model is presented considering symmetry. An open-source IGA package programmed in MATLAB (SIMOGroup 2016) has been adapted in the proposed framework to conduct optimization. The effects of various strength ratios (compressive strength  $f_c$  to tensile strength  $f_t$ ) and minimum width are discussed within this section to demonstrate the construction-oriented concerns. It should be clarified that these attempts are somehow still preliminary regarding the real application of civil engineering structures. The proposed method is conceptually demonstrated using a 2D problem in this paper, which can be extended for 3D formulation later and will be discussed in the follow-up work.

When performing the IGA-SIMP based optimization, the MMA (Svanberg 1987) moving limit of the topology and shape variables are set as 0.1 and 0.01, respectively. The SIMP penalty value is used to accelerate the formation of the configuration of the structure. The penalty is increased from 1.0 to 3.0, with a step size of 0.25 per 25 iterations. A high sharpness value of the erode-and-dilate function  $\beta_{HS}$  strengthens the 0-1 sharpness however, unfavourably reduces optimization stability. Hence, the sharpness value is increased by 1 per 25 iterations from 1 to

5. The tendon-concrete filter width  $\beta_{fl}$  and the sharpness  $\mu_{pre}$  are set as 0.015 and 5.0. A relatively high epsilon-relaxation coefficient  $\varepsilon$  is set as 0.4 to ensure the well-relaxed low-density region, while the aggregation coefficient  $\eta$  is taken as 8.0. The value of  $q_n$  in the STM-based stress correction scheme is fixed to 0.5 to improve the continuity of the aggregated stress evaluation.

## 6.1 Optimization demonstration using simply supported beams

Regarding the material properties of the beams, Young's modulus of the concrete ( $E$ ) is 28 GPa, and Poisson ratio  $\nu=0.2$ . The density of concrete is taken as 2450 kg/m<sup>3</sup>. The load balancing method(Lin and Burns 1981) for curved tendon has been adopted to estimate the tendon force corresponding to given beam geometry. This as an analytical estimation assumes the tendon of a parabola curve, and the prestress force for the beam of length  $L$  is given as:

$$T_{pre} = \frac{q_{sv} L^2}{8a} \quad (39)$$

Where  $q_{sv}$  is the service load (such as vehicles) on the top surface,  $a$  indicates the tendon's drape, set as 0.8 of beam height to ensure a safe distance from tendon to both top and bottom chords.

In this beam example, the beam length  $L$  is 2m, and the height  $D$  is 0.2m. When the service load  $q_{sv}$  equals to 200 kN/m, the analytical  $T_{pre}$  is calculated as 625 kN. According to the IGA result of this rectangular beam, the maximum tensile and compressive stress is 0.28 MPa and 1.33 MPa, respectively, which are both far below the strength limit, indicating low utilization of material capacity in a traditional design. Through utilizing the theoretical prestress force into the proposed optimization method, the restriction of parabolic tendon shape and prismatic concrete topology are eliminated to achieve more efficient tendon shape and lighter concrete beam, which enhancing the practical value of such traditional prestress beam design methods. It should be noted that the concentrated prestress load on the edge is equivalented as a localized pressure to simulate the effect of the anchor and to avoid stress concentration on the loading region.

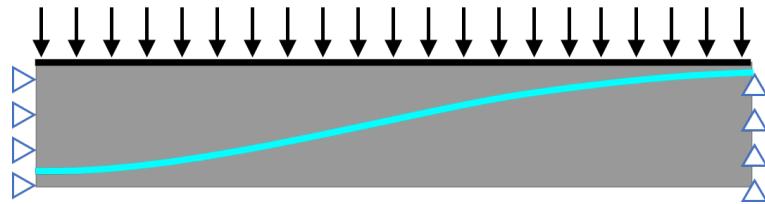


Figure 11 A half model of the simply supported beam with uniform load

The right half of the beam is modelled considering the axial symmetry and discretized as  $200 \times 40$  elements under the IGA framework. For convenient visualization, the half model is duplicated to show a full model in the following discussion. Nine tendon control points are used to generate the curve shape for the prestressed tendon, while 200 knots are inserted to improve the accuracy of load equivalence, as discussed in section 3.2. The elemental density value of the first two upper surface layers is fixed as 1.0 to form a rigid load-carrying surface, and the edge tendon control point is fixed on the upper right corner to predetermine the location of the prestressing anchor, as shown in Figure 11.

Figure 12(a) shows the typical iteration of topology optimization, where the density distribution has been generated after several steps. During the iteration, the structural volume ratio decreases from 1.0 to a converged 0.47, while the D-P criterion value approaches zero, suggesting that the stresses are constrained underneath the yielding surface to remain elastic. The presented optimization is performed with equal strength limits and low minimum-width control (the reference length scale bar can be found in Table 1). Thus, the equal-strength D-P value reflects the Von-Mises stress criterion, and the distribution is shown in Figure 12(b), where the relatively higher level of stresses are in the upper chord. This is due to: (1) the bottom chord assigned with a fixed filter thickness to ensure a sufficient tendon cover; (2) the bottom chord only co-working the tendon to resist the tendon forces, and the main resisting action is taken by the prestressed tendon. Figure 12 presents a visualized topology optimization process without the construction-oriented concerns, whereas the effect of minimum width and unequal strengths is discussed in the following subsections.

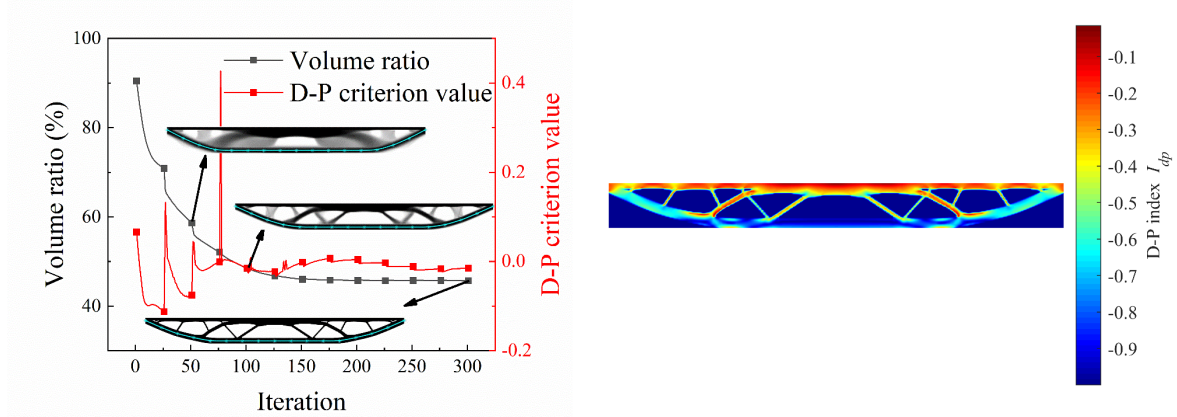


Figure 12 Topology optimization result(equal strength limits, low width control (11.6 mm)): (a) optimization process; (b) the distribution of D-P index ( $I_{dp} = \phi_{F,e} - 1$ ), negative value of  $I_{dp}$  indicates below strength limit.

## 6.2 Effect of different minimum-width control

A NURBS-based minimum length scale control (Costa et al. 2019) is applied to prevent slim components in an optimized structure. As shown in Table 1, the optimized models of various minimum-width control are presented, where the width is selected as 11.6mm, 23.3 mm, and 46.6 mm corresponding to the different density mesh grids:  $100 \times 20$ ,  $50 \times 10$ ,  $25 \times 5$ . In these examples, the compressive strength is taken as 10 MPa, equal to the tensile strength. The iteration of topology correlated to the material distribution during the optimization is shown in Figure 13, in which the variation of volume ratio and D-P value are presented as well. In the optimized models, a density control mesh of  $50 \times 10$  is adopted as the minimum width is limited to 23.3mm.

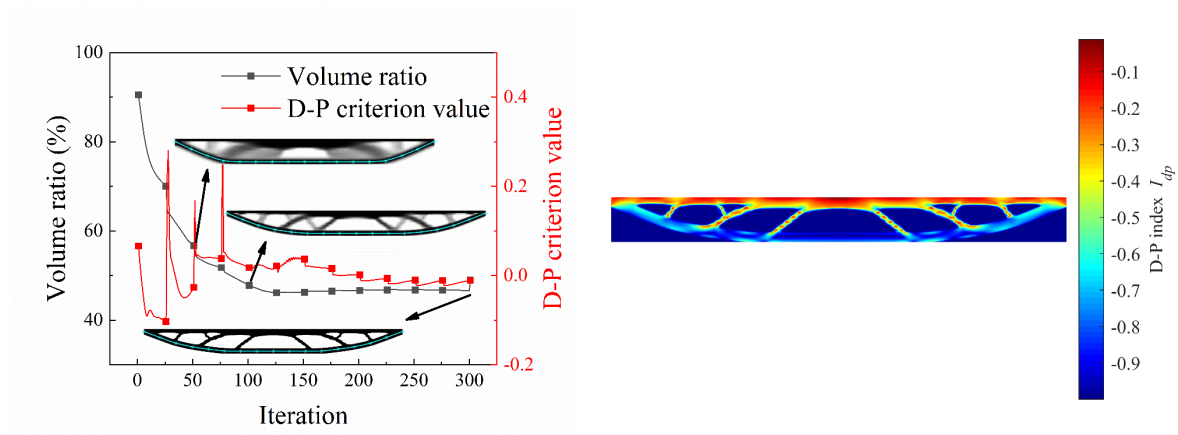
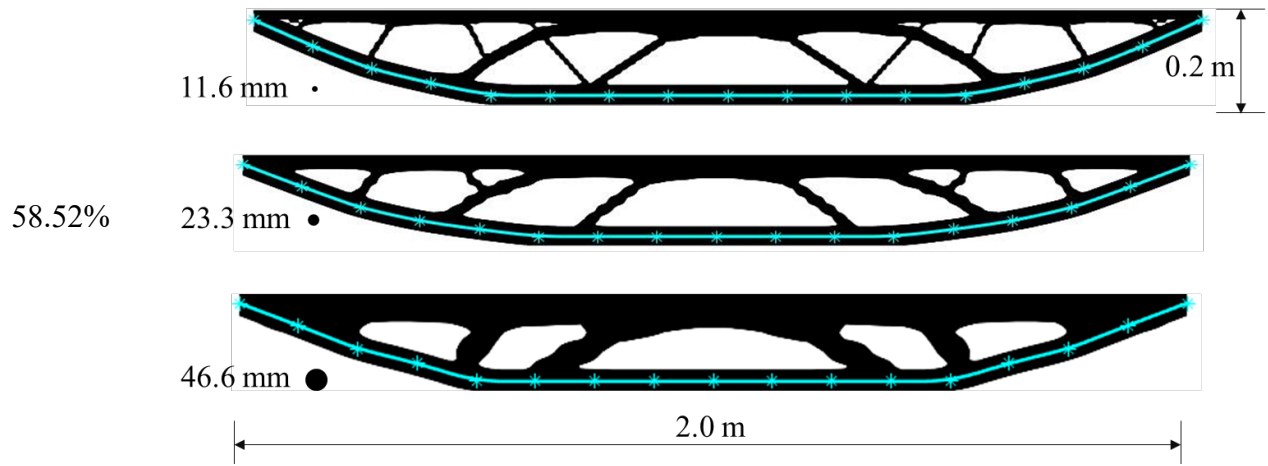


Figure 13 Optimized topology with medium width control (23.3 mm) and equal strength limits: (a) optimization process; (b) the distribution of D-P index  $I_{dp}$ .

Meanwhile, the geometric mesh independent from the density mesh remains as  $200 \times 40$ . When the minimum width limit varies, it can be observed that the slim components and tiny branches are gradually prevented, as shown in Table 1. The structure of a reasonably controlled minimum width thereafter represents a better manufacturability performance for construction.

Table 1 illustration of various minimum-width control in topology optimization

Volume	Configuration
47.39%	
48.91%	



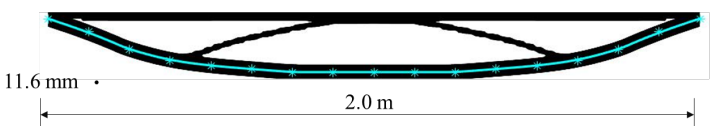


### 6.3 Effect of unequal compressive and tensile strength

Concrete is a common structural material used with steel rebars as reinforcement, which can be either strengthened by adding steel fibers or other types of fibers. The critical feature of concrete is its different strengths in tension and compression. When the tensile strength ( $f_t$ ) and the compressive strength ( $f_c$ ) are known, the topology optimization should maximize the use of the material strength while the safety performance is ensured. As shown in

Table 2, different topology optimization results can be obtained after applying the Drucker-Prager criterion to consider unequal  $f_t$  and  $f_c$ , while a minimum-width control of 11.6 mm is applied in these models. To observe the effect of strength ratios, the compressive and tensile strength are selected as three sets:  $f_c = 10\text{MPa}$ ,  $f_t = 10\text{MPa}$  (Von-Mises Criterion);  $f_c = 13.3\text{MPa}$ ,  $f_t = 6.7\text{MPa}$ ;  $f_c = 15\text{MPa}$ ,  $f_t = 5\text{MPa}$ . Here the scale of summed  $f_c$  and  $f_t$  has been kept the same to represent the similar material capacity combining tension and compression. The optimized structural configuration varies when the ratio of  $f_c / f_t$  is increased from one to three times of tensile strength. As the  $f_c / f_t$  ratio increases, the number of components between the upper and lower chords is reduced because the major components of higher compressive strength can solely bear the load transferred from the chords. Meanwhile, the volume ratio declines from 47.39% to 37.94% as higher compressive strength and  $f_c / f_t$  ratio are employed. It should be noticed that further improvement may be necessary for the optimized structure since the structural performance of the model has to be examined for various loading scenarios considering the service loading and extreme loading, which can lead to additional variation to the optimized topology.

Table 2 Effect of different strength ratio to the topology optimization with low width control (11.6 mm)

Compressive/Tensile Strength	Volume	Configuration
10/10 MPa (1:1)	47.39%	
13.3/6.7 MPa (2:1)	40.89%	
15/5 MPa (3:1)	39.77%	

#### 6.4 Optimized topology under D-P Criterion and width control

When applying the D-P stress constraints, and the minimum-width control simultaneously, the iterative process of topology optimization is illustrated in Figure 14(a). As the strength ratio,  $f_c / f_t$  is set to 3, and the minimum-width control is 23.3mm, the volume ratio and the D-P ratio converge to the optimized values after 300 iterations. Upon the completion of optimization, the obtained shape comprises fewer components and the middle components yield to an arch. Such a regularized shape could significantly simplify the construction procedure, indicating a high level of constructional ability. Figure 14(b) shows the D-P value distribution after the completion of the optimization. When using the same minimum-width control (23.3mm), the variations of optimal topology corresponding to various strength ratios have been shown in Table 3. Comparing to results in Table 2, the optimized models with a minimal width limit of 23.3mm comprises less complexity in terms of the middle component distribution. As a compromising result of the width constraint, higher volume ratios are seen in these optimized models. In real structural design, a balanced performance between the volume ratio (material cost) and the width control (manufacturing cost) should be considered.

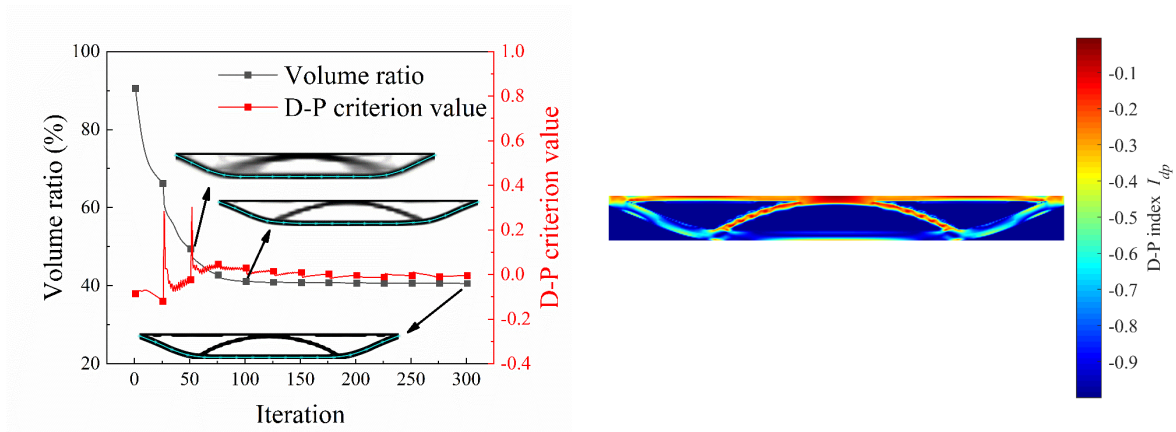


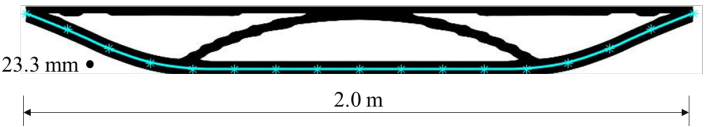


Figure 14 Topology optimization with medium width control and 3:1 strength limit ratio: (a) optimization process; (b) the distribution of D-P index  $I_{dp}$ .

Table 3 Topology optimization results after applying strength ratios and 23mm minimum-width control

<b>Compressive/Tensile Strength</b>	<b>Volume</b>	<b>Configuration</b>
10/10 MPa (1:1)	48.91%	
13.3/6.7 MPa (2:1)	41.04%	
15/5 MPa (3:1)	40.54%	

## 6.5 Optimzation of multiple-span beam cases

To further demonstrate the proposed optimization approach, two continuous beams are briefly presented here, which are of two spans and three spans, respectively. Each span is 2.0m long and similarly configured as the previous single span beam model.  $f_c, f_t$  are adopted as 13.3MPa and 6.7 MPa. The schematic plots of the continuous beams are shown in Figure 15 (a) and (b). The upper surface pressure is assigned as 250kN/m for the continuous beams, and the prestress force is fixed to 625kN. The optimization process and the distribution of D-P index of optimized models are presented in Figure 16.

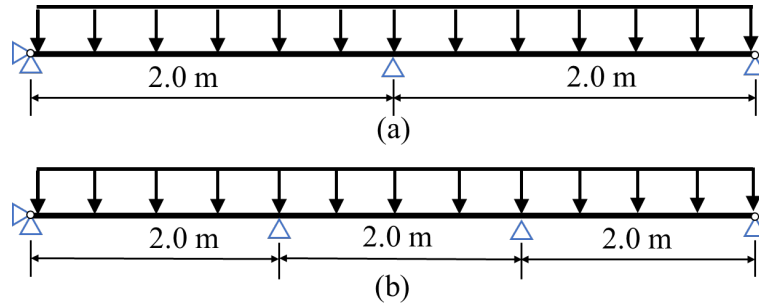


Figure 15 Schematic plot of continuous beams.: (a) a two-span beam ( $2 \times 2.0\text{m}$ ); (b) a three-span beam ( $3 \times 2.0\text{m}$ ).

The optimized models are obtained under the same width control limit as 23.3 mm, while the volume ratios of two beam cases eventually converge at 0.49 and 0.47. As shown in the figures, the tendon profiles of both beams are of smooth curved shapes after the automatic optimization. The tendon-covering region of the stress distribution contours are well below the strength limit, indicating that the prestress tendons effectively alleviate the tensile stress in the



concrete beams. As shown in Figure 16, the optimized topology of continuous beams are of expected performance, which presents well-controlled complexity of component distribution and the well-achieved efficiency in pursuing a lightweight design.

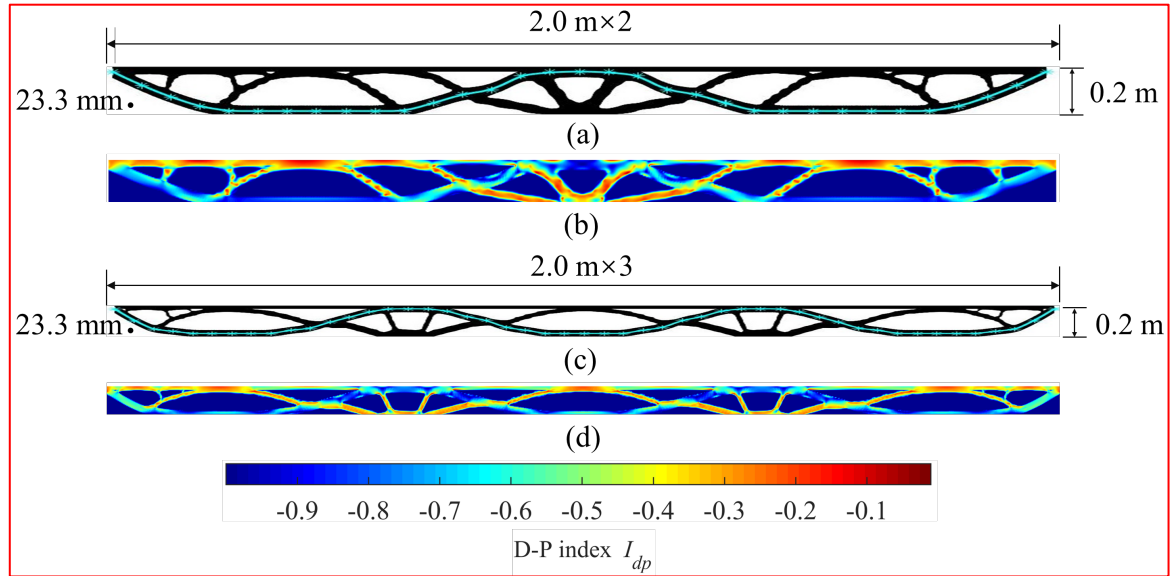


Figure 16 Topology optimization process of two-span beam: (a) density distribution of two-span beam; (b) D-P index  $I_{dp}$  distribution of two-span beam; (c) density distribution of three-span beam; (d) D-P index  $I_{dp}$  distribution of three-span beam

## 7. Conclusion

In this paper, an IGA-SIMP topology optimization approach has been developed along with a vision of a construction-oriented topology optimization framework. The constraint functions for material stresses and geometric configuration have been implemented to address safety and manufacturability in real construction practice.

A prestressed concrete beam comprising a steel tendon and a concrete beam is modelled and optimized using the proposed topology optimization framework. The NURBS-IGA based mapping from the tendon to the concrete entity can achieve a simultaneous optimization over the concrete topology and the tendon curve shape. The Drucker-Prager criterion has been applied to consider the unequal strength limits for tension and compression as commonly encountered for concrete-type materials in real construction. A minimum-width control is implemented during the topology optimization to prevent very slim components in the optimum model.

The effect of strength ratio  $f_c / f_t$  and minimum width has been demonstrated using the prestressed concrete beam. The increasing strength ratio can lead to a different distribution of concrete in the optimized beam and a lower volume ratio. When applying minimum-width

control, the branch components are significantly reduced, and the pattern of internal components tends to be more regularized, which could essentially improve the manufacturability of the optimized structures.

As discussed in this paper, the construction-oriented constraint functions are not limited to the stress criterion and width control. To implement topology optimization in structural engineering, the performance of the optimized structure subjected to various loading scenarios during its life-time service should be considered. The manufacturing cost and the maintenance cost (i.e., resilience) of the structure should also be taken into account. These concerns should be plugged into the construction-oriented topology optimization framework, and the future work of the authors will continue to explore it.

## 8. Appendix

### 8.1 The curvature sensitivity analysis of the tendon curve

The formulation of curvature can be written as:

$$\kappa(\xi) = \frac{|\mathbf{C}'(\xi) \times \mathbf{C}''(\xi)|}{|\mathbf{C}'(\xi)|^3} = \frac{|\mathbf{A}|}{|\mathbf{B}|^3} \quad (40)$$

where  $\mathbf{C}'(\xi), \mathbf{C}''(\xi)$  are the first and second derivative values of the tendon curve, respectively. For the sake of formulation simplicity, we define terms  $\mathbf{A} = \mathbf{C}'(\xi) \times \mathbf{C}''(\xi)$  and  $\mathbf{B} = \mathbf{C}'(\xi)$ . Therefore, the expression of Eq. (40) could be rewritten as:

$$\frac{\partial \kappa(\xi)}{\partial y_i} = \frac{\mathbf{A}}{|\mathbf{A}||\mathbf{B}|^3} \frac{\partial \mathbf{A}}{\partial y_i} - \frac{3\mathbf{B}|\mathbf{A}|}{|\mathbf{B}|^5} \frac{\partial \mathbf{B}}{\partial y_i} \quad (41)$$

where the term  $\frac{\partial \mathbf{A}}{\partial y_i}$  is resulted in  $\frac{\partial \mathbf{A}}{\partial y_i} = \frac{\partial \mathbf{C}'(\xi)}{\partial y_i} \times \mathbf{C}''(\xi) + \mathbf{C}'(\xi) \times \frac{\partial \mathbf{C}''(\xi)}{\partial y_i}$ ; and the term

$\frac{\partial \mathbf{B}}{\partial y_i}$  is straightforward:  $\frac{\partial \mathbf{B}}{\partial y_i} = \frac{\partial \mathbf{C}'(\xi)}{\partial y_i}$ .

According to the formulation of the first and second derivative values of the tendon curve, the corresponding derivatives are given as follows:

$$\begin{aligned} \frac{\partial \mathbf{C}'(\xi)}{\partial y_i} &= \sum_{j=1}^{N_{refine}} \left( \frac{\partial R_{j,p}^{tendon}(\xi)}{\partial \xi} \frac{\partial \mathbf{P}_j^{tendon}}{\partial y_i} \right) \\ \frac{\partial \mathbf{C}''(\xi)}{\partial y_i} &= \sum_{j=1}^{N_{refine}} \left( \frac{\partial^2 R_{j,p}^{tendon}(\xi)}{\partial \xi^2} \frac{\partial \mathbf{P}_j^{tendon}}{\partial y_i} \right) \end{aligned} \quad (42)$$

## 8.2 Normal direction sensitivity analysis of the tendon curve

The formulation of normal direction can be written as:

$$\mathbf{n}(\xi) = \begin{bmatrix} 0 & 1 \\ -1 & 0 \end{bmatrix} * \begin{bmatrix} \cos \theta_\xi \\ \sin \theta_\xi \end{bmatrix} \quad (43)$$

where  $\theta_\xi$  represents the angle at the location  $\xi$ , and the expression could further take the

form as  $\begin{bmatrix} \cos \theta_\xi \\ \sin \theta_\xi \end{bmatrix} = \frac{d\mathbf{x}(\xi)}{ds} = \frac{\mathbf{J}_1^{tendon}}{|\mathbf{J}_1^{tendon}|}$ . Therefore, the derivative of normal  $\frac{\partial \mathbf{n}(\xi)}{\partial y_i}$  and is as

below:

$$\frac{\partial \mathbf{n}(\xi)}{\partial y_i} = \begin{bmatrix} 0 & 1 \\ -1 & 0 \end{bmatrix} * \left( \frac{1}{|\mathbf{J}_1^{tendon}|} - \frac{(\mathbf{J}_1^{tendon})^2}{|\mathbf{J}_1^{tendon}|^3} \right) \frac{\partial \mathbf{J}_1^{tendon}}{\partial y_i} \quad (44)$$

Likewise, the tangential direction  $\frac{\partial \mathbf{n}^*}{\partial y_i}$  can be written as:

$$\frac{\partial \mathbf{n}^*}{\partial y_i} = \left( \frac{1}{|\mathbf{J}_1^{tendon}|} \frac{\partial \mathbf{J}_1^{tendon}}{\partial y_i} - \frac{\mathbf{J}_1^{tendon}}{|\mathbf{J}_1^{tendon}|^2} \frac{\partial |\mathbf{J}_1^{tendon}|}{\partial y_i} \right) \quad (45)$$

where  $\mathbf{J}_1^{tendon}$  is the tendon elemental Jacobian matrix from physical space to parametric space is calculated by:

$$\mathbf{J}_1^{tendon} = \sum_{j \in e} \frac{\partial R_j^{ten}(e)}{\partial \xi} \mathbf{P}_j^{refine} \quad (46)$$

and the corresponding derivatives term  $\frac{\partial \mathbf{J}_1^{tendon}}{\partial y_i}$  is:

$$\frac{\partial \mathbf{J}_1^{tendon}}{\partial y_i} = \sum_{j \in e} \frac{\partial R_{j,p}^{tendon}(e)}{\partial \xi} \frac{\partial \mathbf{P}_j^{refine}}{\partial y_i} \quad (47)$$

According to Eq. (14), the term  $\frac{\partial \mathbf{P}_j^{refine}}{\partial y_i}$  in Eq. (47) can be given as:

$$\frac{\partial \mathbf{P}_j^{refine}}{\partial y_i} = \frac{\partial \mathbf{P}_j^{refine}}{\partial y_j^{refine}} \frac{\partial y_j^{refine}}{\partial y_i} = W_{j,i}^{refine} \frac{\partial \mathbf{P}_j^{refine}}{\partial y_j^{refine}} \quad (48)$$

where the corresponding derivative is set as  $\frac{\partial \mathbf{P}_j^{refine}}{\partial y_j^{refine}} = [0, 1, 0]$ . Furthermore, the derivative term

$\frac{\partial |\mathbf{J}_1^{tendon}|}{\partial y_i}$  is calculated by:

$$\frac{\partial |\mathbf{J}_1^{tendon}|_e}{\partial y_i} = \frac{(\mathbf{J}_1^{tendon})_e}{|\mathbf{J}_1^{tendon}|_e} \frac{\partial (\mathbf{J}_1^{tendon})_e}{\partial y_i} \quad (49)$$

## Acknowledgment

The first author would like to acknowledge the financial support of the RISUD Ph.D. studentship and the corresponding author would like to acknowledge the support from the Start-up Funding of the Hong Kong Polytechnic University (P0031564).

## Conflict of interest

The authors declare that no conflict of interest is encountered in this paper.

## Replication of results

MATLAB codes for the simply supported prestressed concrete beam optimized with 23 mm width control and 3:1 strength limit ratio is provided as supplementary materials to the journal. To ease the concern of program convergence, the effect of specific parameters are introduced here: (1) the step-up of penalty  $p$  accelerates the formation of optimized topology; (2) too high  $\beta_{HS}$  do affect the convergence stability, a reasonable range is recommended (Amir and Shakour 2018); (3) the width of full-cover tendon filter  $\beta_{fil}$  is irrelevant to convergence problem; (4) the range of tendon-concrete filter sharpness  $\mu_{pre}$  is also recommended (Amir and Shakour 2018); (5) the epsilon-relaxation coefficient  $\varepsilon$  is a recommended value (Cheng and Guo 1997); (6) the value aggregation coefficient  $\eta$  and STM-based stress correction scheme  $q_n$  are both recommended (Yang et al. 2018). **The parameters used in this paper are determined according to these recommendations and similar process can be applied to other case studies.**

## References

- Almeida VS, Simonetti HL, Neto LO (2013) Comparative analysis of strut-and-tie models using Smooth Evolutionary Structural Optimization. *Engineering Structures* 56:1665-1675
- Amir O (2013) A topology optimization procedure for reinforced concrete structures. *Computers & Structures* 114:46-58
- Amir O, Shakour E (2018) Simultaneous shape and topology optimization of prestressed concrete beams. *Structural and Multidisciplinary Optimization* 57:1831-1843 doi:10.1007/s00158-017-1855-5

- Amir O, Sigmund O (2013) Reinforcement layout design for concrete structures based on continuum damage and truss topology optimization. *Structural and Multidisciplinary Optimization* 47:157-174
- Beghini LL, Beghini A, Baker WF, Paulino GH (2015) Integrated discrete/continuum topology optimization framework for stiffness or global stability of high-rise buildings *Journal of Structural Engineering* 141:04014207
- Bogomolny M, Amir O (2012) Conceptual design of reinforced concrete structures using topology optimization with elastoplastic material modeling. *International journal for numerical methods in engineering* 90:1578-1597
- Bruggi M (2009) Generating strut-and-tie patterns for reinforced concrete structures using topology optimization. *Computers & Structures* 87:1483-1495
- Bruggi M (2010) On the automatic generation of strut and tie patterns under multiple load cases with application to the aseismic design of concrete structures. *Advances in Structural Engineering* 13:1167-1181
- Bruggi M (2016) A numerical method to generate optimal load paths in plain and reinforced concrete structures. *Computers & Structures* 170:26-36
- Bruggi M, Duysinx P (2012) Topology optimization for minimum weight with compliance and stress constraints *Structural and Multidisciplinary Optimization* 46:369-384
- Bruggi M, Taliervo A (2013) Topology optimization of the fiber-reinforcement retrofitting existing structures. *International Journal of Solids and Structures* 50:121-136
- Cheng GD, Guo X (1997)  $\epsilon$ -relaxed approach in structural topology optimization. *Structural Optimization* 13:258-266 doi:10.1007/BF01197454
- Costa G, Montemurro M, Pailhès J (2019) Minimum length scale control in a NURBS-based SIMP method *Computer Methods in Applied Mechanics and Engineering* 354:963-989
- Deaton JD, Grandhi RV (2014) A survey of structural and multidisciplinary continuum topology optimization: post 2000. *Structural and Multidisciplinary Optimization* 49:1-38 doi:10.1007/s00158-013-0956-z
- Duysinx P, Sigmund O New developments in handling stress constraints in optimal material distribution. In: 7th AIAA/USAF/NASA/ISSMO Symposium on Multidisciplinary Analysis and Optimization, 1998.
- Eschenauer HA, Olhoff N (2001) Topology optimization of continuum structures: a review. *Appl Mech Rev* 54:331-390
- Eurviriyankul S, Askes H (2011) Tendon layout optimisation through configurational forces equilibration in plane stress analysis of prestressed concrete structures. *Computers & structures* 89:1673-1680
- Gao J, Gao L, Luo Z, Li P (2019) Isogeometric topology optimization for continuum structures using density distribution function *International Journal for Numerical Methods in Engineering* 119:991-1017
- Gaynor AT, Guest JK, Moen CD (2013) Reinforced concrete force visualization and design using bilinear truss-continuum topology optimization. *Journal of Structural Engineering* 139:607-618
- Hughes TJ, Cottrell JA, Bazilevs Y (2005) Isogeometric analysis: CAD, finite elements, NURBS, exact geometry and mesh refinement. *Computer methods in applied mechanics and engineering* 194:4135-4195
- Jewett JL, Carstensen JV (2019) Topology-optimized design, construction and experimental evaluation of concrete beams. *Automation in Construction* 102:59-67
- Jiang L, Jiang Y, Zhang Z, Usmani A (2021) Thermal Analysis Infrastructure in OpenSees for Fire and its Smart Application Interface Towards Natural Fire Modelling *Fire Technology*:1-26

- Jiang L, Usmani A (2018a) Computational performance of beam-column elements in modelling structural members subjected to localised fire. *Engineering Structures* 156:490-502
- Jiang L, Usmani A (2018b) Towards scenario fires—modelling structural response to fire using an integrated computational tool. *Advances in structural engineering* 21:2056-2067
- Kwak H-G, Noh S-H (2006) Determination of strut-and-tie models using evolutionary structural optimization. *Engineering Structures* 28:1440-1449
- Lazarov BS, Wang F, Sigmund O (2016) Length scale and manufacturability in density-based topology optimization. *Archive of Applied Mechanics* 86:189-218 doi:10.1007/s00419-015-1106-4
- Liang QQ, Xie YM, Steven GP (2000) Topology optimization of strut-and-tie models in reinforced concrete structures using an evolutionary procedure., American Concrete Institute
- Lin TY, Burns NH (1981) Design of prestressed concrete structures
- Liu H, Yang D, Hao P, Zhu X (2018) Isogeometric analysis based topology optimization design with global stress constraint. *Computer Methods in Applied Mechanics and Engineering* 342:625-652
- Luo Y, Kang Z (2013) Layout design of reinforced concrete structures using two-material topology optimization with Drucker-Prager yield constraints. *Structural and Multidisciplinary Optimization* 47:95-110 doi:10.1007/s00158-012-0809-1
- Moorman RB (1952) Equivalent load method for analyzing prestressed concrete structures. University of Missouri,
- Piegl L, Tiller W (2012) The NURBS book. Springer Science & Business Media,
- Rozvany GIN (2009) A critical review of established methods of structural topology optimization. *Structural and Multidisciplinary Optimization* 37:217-237 doi:10.1007/s00158-007-0217-0
- Sigmund O, Maute K (2013) Topology optimization approaches. *Structural and Multidisciplinary Optimization* 48:1031-1055 doi:10.1007/s00158-013-0978-6
- SIMOGROUP (2016) SIMO-Package, a basic NURBS-based IsoGeometric Analysis package written in MATLAB. <https://github.com/SIMOGROUP/SIMO-Package>.
- Stromberg LL, Beghini A, Baker WF, Paulino GH (2011) Application of layout and topology optimization using pattern gradation for the conceptual design of buildings *Structural and Multidisciplinary Optimization* 43:165-180
- Stromberg LL, Beghini A, Baker WF, Paulino GH (2012) Topology optimization for braced frames: combining continuum and beam/column elements *Engineering Structures* 37:106-124
- Svanberg K (1987) The method of moving asymptotes—a new method for structural optimization. *International Journal for Numerical Methods in Engineering* 24:359-373 doi:10.1002/nme.1620240207
- Vantghem G, De Corte W, Shakour E, Amir O (2020) 3D printing of a post-tensioned concrete girder designed by topology optimization. *Automation in Construction* 112:103084
- Verbart A, Langelaar M, Keulen FV (2017) A unified aggregation and relaxation approach for stress-constrained topology optimization. *Structural & Multidisciplinary Optimization*
- Yang D, Liu H, Zhang W, Li S (2018) Stress-constrained topology optimization based on maximum stress measures. *Computers & Structures* 198:23-39
- Yang RJ, Chen CJ (1996) Stress-based topology optimization. *Structural and Multidisciplinary Optimization* 12:98-105

